JACS
JOURNAL OF THE AMERICAN CHEMICAL SOCIETY
pubs.acs.org/JACS
Article

Open Access
This article is licensed under CC-BY 4.0

Steering the Absorption Configuration of Intermediates over Pd-Based Electrocatalysts toward Efficient and Stable CO_2 Reduction

Shuting Wei, Yanchao Xu, Tao Song, Hao Dai, Fan Li, Xin Gao, Yanjie Zhai, Shanhe Gong, Rui Li, Xiao Zhang,* and Kangcheung Chan*

Cite This: J. Am. Chem. Soc. 2025, 147, 4219–4229

Read Online

ACCESS | Metrics & More | Article Recommendations | Supporting Information

ABSTRACT: Palladium (Pd) catalysts are promising for electrochemical reduction of CO_2 to CO but often can be deactivated by poisoning owing to the strong affinity of *CO on Pd sites. Theoretical investigations reveal that different configurations of *CO endow specific adsorption energies, thereby dictating the final performances. Here, a regulatory strategy toward *CO absorption configurations is proposed to alleviate CO poisoning by simultaneously incorporating Cu and Zn atoms into ultrathin Pd nanosheets (NSs). As-prepared PdCuZn NSs can catalyze CO production at a wide potential window (−0.28 to −0.78 V vs RHE) and achieve a maximum FE_{CO} of 96% at −0.35 V. Impressively, it exhibits stable CO production of 100 h under ∼95% FE_{CO} with no decay. Combined results from X-ray analysis, in situ spectroscopy, and theoretical simulations suggest that the codoping strategy not only optimizes the electronic structure of Pd but also weakens the binding strengths of *CO and increases the proportion of weak-binding linear *CO absorption configuration on catalysts' surfaces. Such targeted adoption of weakly bound configurations abates the energy barrier of *CO desorption and facilitates CO production. This work confers a useful design tactic toward Pd-based electrocatalysts, codoping for steering adsorption configuration to achieve highly selective and stable CO_2-to-CO conversion.

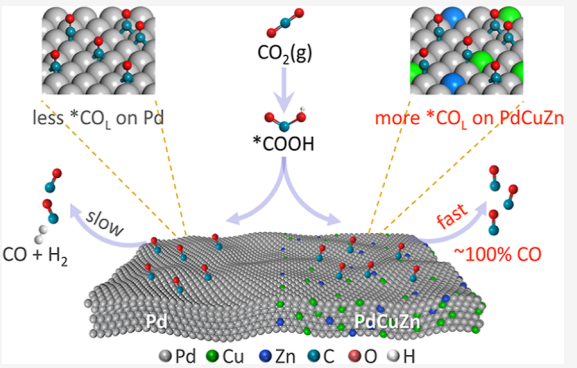

1. INTRODUCTION

Electrochemical CO_2 reduction into value-added chemicals and fuels powered by renewable electricity represents a promising approach to alleviate the carbon emission issue, balance the future carbon cycle, and eventually establish a sustainable energy economy.[1−4] Multiple products ranging from C_1 to C_{3+} oxygenates and hydrocarbons can be obtained via the CO_2 reduction reaction (CO_2RR).[5−11] Among various products, CO has attracted widespread attention due to its sizable market and economic feasibility.[12−14] To date, many metal candidates (such as Cu, Ag, Au, Zn) have been studied for CO_2-to-CO conversion, in which Pd exhibits potential for CO formation because of its facile CO_2 absorption and *COOH formation.[15,16] Unfortunately, the strong *CO binding on the Pd surface makes the subsequent *CO desorption a sluggish step and results in severe poisoning of active sites, finally deactivating the CO_2-to-CO conversion within hours.[17,18] The development of efficient Pd-catalysts with a suitable *CO binding energy still needs substantial improvements.

The binding strength of reaction intermediates is determined by the specific adsorption behaviors.[19,20] Theoretical studies have shown that there are three types of *CO configurations including linearly bound (CO_L), bridge bound (CO_B), and triple bound (CO_T) on metal surfaces.[21] As summarized in Scheme 1a, the binding strength of *CO on the Pd(111) surface gives a sequence of $*CO_L$ (−1.29 eV) < $*CO_B$ (−1.77 eV) < $*CO_T$ (−1.95 eV),[22] which makes $*CO_L$ favorable for the subsequent desorption from Pd sites. The specific absorption behavior of reaction intermediates can be influenced by the electronic structure of active sites,[23,24] which provides possibilities to tailor the adsorption configurations via subtle electronic regulations. Alloying represents a powerful tool to modify the catalyst's electronic structure,[25,26] in which the shifts of metal d-band are closely related to the binding affinity of intermediates on active sites.[27,28] Such regulating tactics have been widely utilized as the general design principles of bimetallic Pd alloys with refined electronic structures, resulting in high selectivity of Pd-based alloys for CO_2RR.[29−32] However, the impact of Pd alloying toward detailed adsorption behaviors, especially the influence of alloying Pd with multiple metals toward specific adsorption configurations of key reaction intermediates, is scarcely

Received: October 10, 2024
Revised: January 12, 2025
Accepted: January 13, 2025
Published: January 24, 2025

Downloaded via HONG KONG POLYTECHNIC UNIV on February 28, 2025 at 02:53:59 (UTC).
See https://pubs.acs.org/sharingguidelines for options on how to legitimately share published articles.

ACS Publications
© 2025 The Authors. Published by American Chemical Society

https://doi.org/10.1021/jacs.4c14253
J. Am. Chem. Soc. 2025, 147, 4219−4229

Scheme 1. (a) Specific Binding Energies of *CO with Different Configurations on the Pd(111) Surface; (b) Schematic Illustration Showing the Impact of Cu/Zn Incorporation on the CO_2-to-CO Process

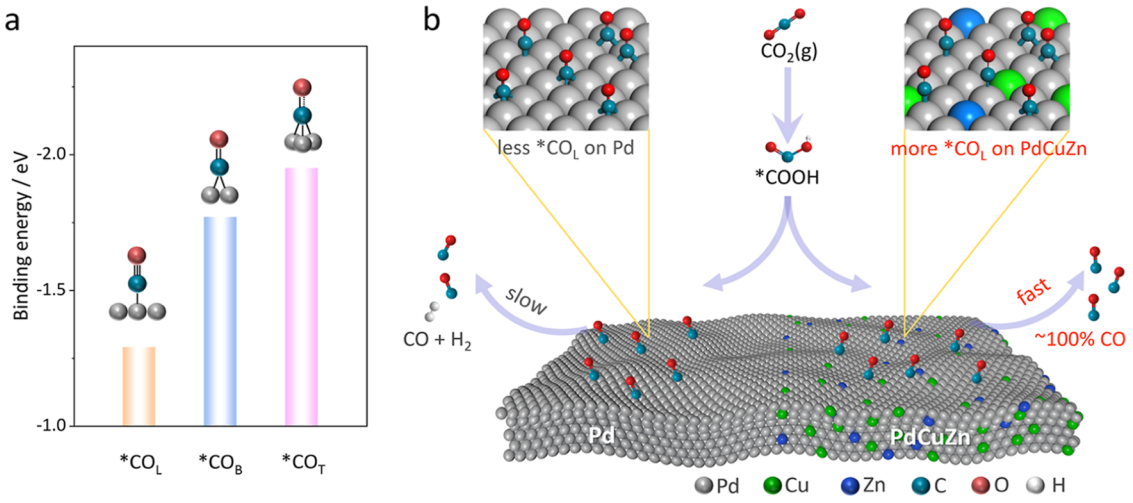

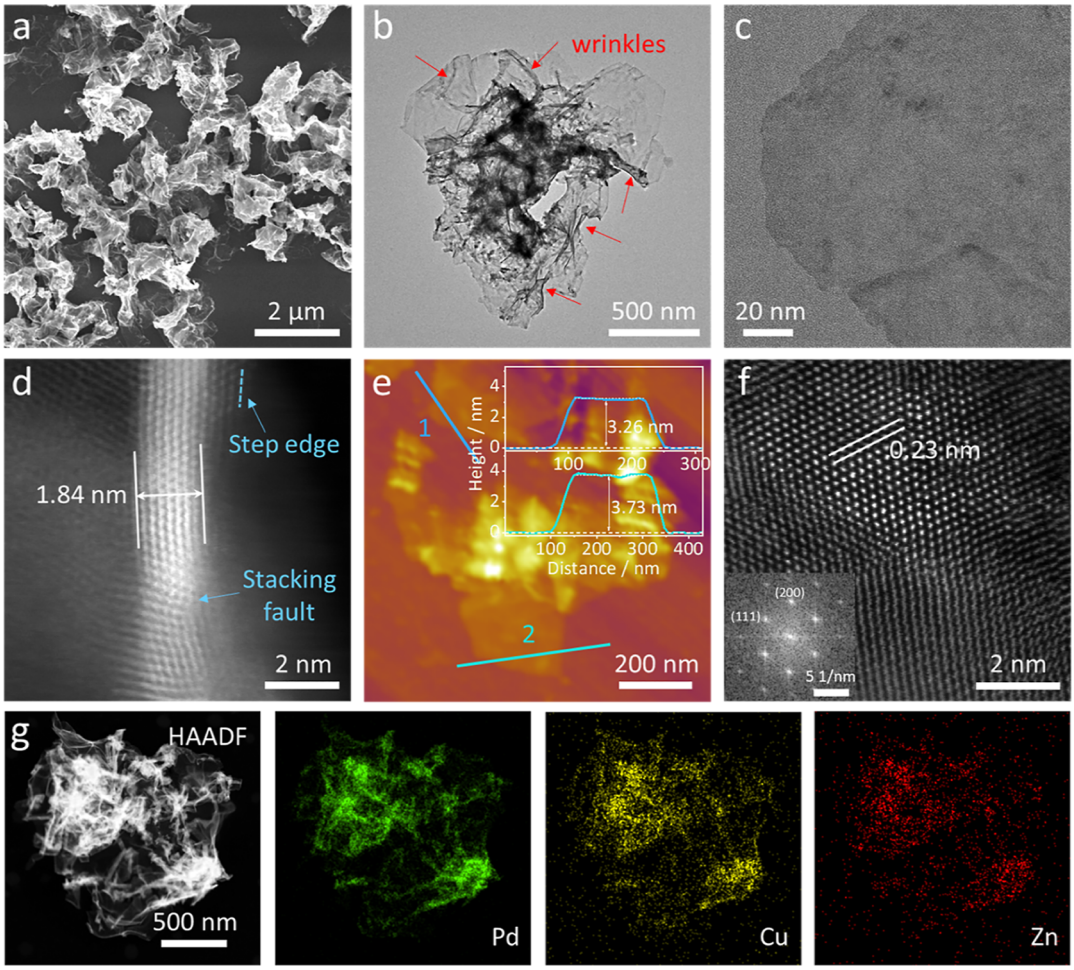

Figure 1. Morphology and structure characterization of PdCuZn NSs. (a) SEM image, (b,c) TEM images, (d) HAADF-STEM image, (e) AFM image (inset: the corresponding height profiles of the PdCuZn NSs), (f) high-resolution HAADF-STEM image, and (g) EDS elemental mappings.

explored, which is believed to be the intrinsic factor in determining the final activities.

Two-dimensional ultrathin metals show a large surface area and expose the active sites to a great extent, which provides an ideal platform to study the influences of alloying-induced electronic coupling and strain effects on adsorption behaviors.[33−35] Cu and Zn have different electronic structures and CO adsorption ability from Pd. Introducing Cu with suitable *CO binding interaction into Pd helps to reduce the energy barrier between the intermediate and substrate.[30,36] Zn is located on the weakly bound side of the volcano apex, which is conducive to CO desorption.[37] The simultaneous introduction

https://doi.org/10.1021/jacs.4c14253
J. Am. Chem. Soc. 2025, 147, 4219−4229

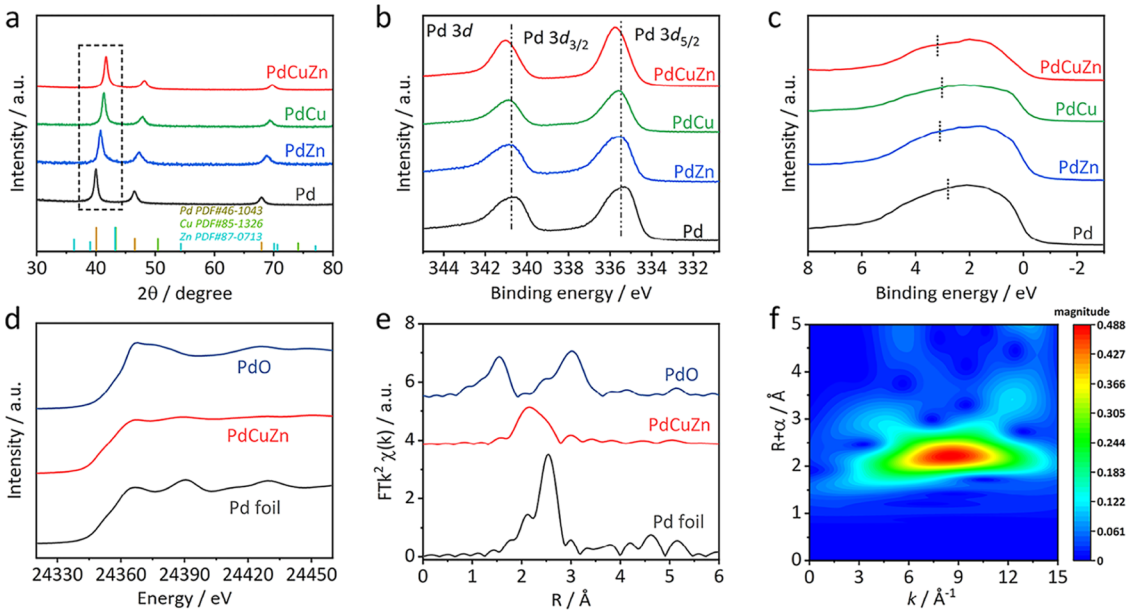

Figure 2. Crystal and electronic structure analysis. (a) XRD patterns, (b) Pd 3d XPS spectra, and (c) the valence band spectra of different samples. (d) XANES spectra, (e) FT-EXAFS spectra of the Pd K-edge region, and (f) WT-EXAFS pattern at the Pd K-edge for PdCuZn NSs.

of Cu and Zn into Pd is expected to greatly optimize the electronic structure and alleviate the absorption strength of CO on Pd. Therefore, in this work, the ultrathin Pd alloy nanosheets (NSs) are designed and fabricated for boosting electrocatalytic CO_2-to-CO conversion by Cu and Zn coincorporation. The as-prepared PdCuZn NSs with few atomic layers exhibit remarkable activity and selectivity toward CO production from CO_2RR, which shows a maximum Faradaic efficiency (FE_{CO}) of 96% at −0.35 V (vs RHE), far more superior than that of PdCu (80% FE_{CO}) and PdZn (65% FE_{CO}) alloys. Thanks to the strong electronic coupling between multiple components and ultrathin structures, PdCuZn NSs also exhibit excellent long-term stability of 100 h electrolysis without current and selectivity loss. The membrane electrode assembly test of as-prepared PdCuZn NSs also shows stable FE_{CO} (~80%) under −200 mA cm^{-2} for 45 h, suggesting their promising potentials in terms of practical conditions. Experimental results manifest that simultaneous codoping of Cu and Zn optimizes the catalyst's electronic structure and lowers the d-band center, which effectively regulates the binding affinity of reaction intermediates on the Pd surface. In situ electrochemical spectroscopy analysis and density functional theory simulations reveal that the introduction of Cu and Zn not only steers the adsorption configurations of *CO on the Pd sites but also weakens the bonding strength of *CO on Pd sites. As illustrated in Scheme 1b, by the codoping of Cu and Zn, the key *CO intermediates on PdCuZn are more likely to adopt the linear $*CO_L$ configuration (with weak CO binding) instead of the dominant triple-bonded configuration (with strong CO binding) on pure Pd, which finally weakens the *CO binding on Pd sites. The alleviated CO poisoning of Pd expedites the rate-determining *CO desorption process and finally facilitates the selective conversion of the CO_2RR to CO products.

2. RESULTS AND DISCUSSION

The structural information on Cu- and Zn-codoped Pd alloys (PdCuZn) was first characterized by scanning electron microscopy (SEM) and transmission electron microscopy (TEM). In Figure 1a, the SEM image of as-prepared PdCuZn alloys exhibits irregular and undulant NS morphology with sizes ranging from one to several micrometers. The low-magnification TEM image in Figure 1b shows abundant wrinkles and corrugations on the NSs. The corrugated characteristic implies a flexible and ultrathin nature of the PdCuZn NSs, which is confirmed by the low contrast of single NS in the high-magnification TEM image (Figure 1c). The side view of a selected NS in a high-angle annular dark-field scanning transmission electron microscopy (HAADF-STEM) image (Figure 1d) shows that the thickness is as low as 1.84 nm, which is equivalent to about eight atomic layers. The thickness of the NSs is further determined to be ~3−4 nm by atomic force microscopy (AFM) in Figure 1e. The height profiles of two randomly selected regions show specific thicknesses of 3.26 and 3.73 nm, respectively, which are thicker than those measured by an electron microscope, probably due to the possible stacking and the adsorbed capping agent on the NSs.[38] As shown in Figure 1f, the aberration-corrected HAADF-STEM image shows clear lattice fringes with an interplanar spacing of 0.23 nm, corresponding to 1/3 (422) of the face-centered cubic (fcc) Pd, manifesting the emergence of stacking faults parallel to the basal (111) planes associated with the Pd NSs.[39,40] The fast Fourier transform (FFT) pattern (inset of Figure 1f) also manifests the fcc crystal structure with a predominant (111) plane of the as-resulting PdCuZn NSs. Elemental mapping analysis in Figure 1g reveals the homogeneous distribution of Pd, Cu, and Zn throughout the selected NSs, indicating their alloy character. The composition ratio of Pd/Cu/Zn in PdCuZn NSs is calculated to be 3.99/1.96/1.00 by inductively coupled plasma-optical emission spectroscopy (ICP-OES) (Table S1). In addition, the pure Pd NSs, Cu-doped Pd NSs (defined as PdCu NSs), and Zn-doped Pd NSs (defined as PdZn NSs) were also prepared as references to investigate the influences of multiple components toward the CO_2RR. Their detailed

https://doi.org/10.1021/jacs.4c14253
J. Am. Chem. Soc. 2025, 147, 4219−4229

structural analysis can be found in the Supporting Information in Figures S1−S3.

The crystal structure of as-prepared samples was analyzed by X-ray diffraction (XRD). As exhibited in Figure 2a, pure Pd NSs show three typical diffraction peaks at 39.9°, 46.5°, and 67.9°, assigned to (111), (200), and (220) planes of Pd with a fcc structure. The PdCuZn, PdCu, and PdZn NSs display the same fcc structure as Pd NSs, in which their diffraction peaks shift to higher angles compared with pure Pd, confirming their alloy nature. Notably, the diffraction peaks of PdCuZn NSs demonstrate a more positive shift when compared with PdCu and PdZn NSs, which is attributed to the coincorporation of Cu and Zn with a small atom radius. Such codoping results in stronger compressive strain in the Pd lattice than that of bimetallic counterparts, which probably changes the electronic structure of Pd and affects the binding of absorbed species on active sites more efficiently. X-ray photoelectron spectroscopy (XPS) was performed to further study the effects of Cu/Zn doping on the electronic structure of the Pd sites. As shown in Figure S4, the Pd 3d XPS spectrum of PdCuZn NSs displays two peaks, corresponding to the spin−orbit double peak of Pd $3d_{5/2}$ and Pd $3d_{3/2}$, respectively. The peaks at 335.77 and 341.02 eV are attributed to Pd^0 $3d_{5/2}$ and Pd^0 $3d_{3/2}$, while the peaks at 337.15 and 342.90 eV belong to Pd^{2+} $3d_{5/2}$ and Pd^{2+} $3d_{3/2}$, respectively. In the comparison of PdCu, PdZn, and Pd NSs, the Pd 3d XPS spectrum of PdCuZn NSs shifts to a higher binding energy (Figure 2b). The positive shift of Pd binding energy indicates that the d-band center is far away from the Fermi level,[31,41] which is beneficial for diminishing the binding affinity of key intermediates and improving the catalytic performance for the CO_2RR. For the Cu 2p XPS spectrum of PdCuZn NSs, the peaks at 931.85 and 951.60 eV belong to Cu^0 $2p_{5/2}$ and Cu^0 $2p_{3/2}$, respectively, while the peaks at 933.85 and 953.60 eV correspond to Cu^{2+} $2p_{5/2}$ and Cu^{2+} $2p_{3/2}$, respectively. The Cu 2p XPS spectrum of PdCuZn NSs shifts to a lower binding energy than that of PdCu NSs. A similar phenomenon occurs in Zn 2p XPS spectra (Figure S5). These results demonstrate that the simultaneous introduction of bimetallic atoms greatly modifies the electronic structure of Pd. The d-band center is quantitatively determined by the XPS valence band spectra. As shown in Figure 2c, the d-band centers of PdCuZn, PdCu, and PdZn NSs are estimated to be 3.20, 3.07, and 3.14 eV, respectively. All alloyed Pd NSs shift away from the Fermi level when compared with pure Pd (2.84 eV), among which PdCuZn NSs have the lowest d-band center. The most dramatic downshift over the d-band might contribute to reducing the absorption between the active sites and reactants or key intermediates, thus dictating the catalytic performance of catalysts.[42−44]

The valence states and coordination circumstances of PdCuZn NSs were further investigated by X-ray absorption spectroscopy (XAS). The X-ray absorption near-edge structure (XANES) of each metal element in PdCuZn NSs is shown in Figures 2d and S6a,b, respectively. The absorption spectra of Pd, Cu, and Zn K-edges of PdCuZn NSs coincide well with those of metal foils, indicating that Pd, Cu, and Zn in PdCuZn NSs mainly exist in the metallic valence state, which is in accordance with the XPS results. The Fourier transform EXAFS (FT-EXAFS) spectrum of the Pd K-edge region for PdCuZn NSs in Figure 2e exhibits a main peak at 2.20 Å, assigned to the nearest Pd−M bond (M = Pd, Cu, or Zn). The bond distance of the Pd−M bond is shorter than that of the Pd−Pd bond (2.54 Å) of Pd foil, signifying the existence of compressive strain in the lattice due to the doping of Cu and Zn atoms, in good agreement with the XRD results. According to previous reports, the compressive strain will lower the d-band center and in turn weaken the binding toward reaction intermediates.[45,46] The FT-EXAFS spectrum of Pd in PdCuZn NSs also shows an obvious decrease in the intensity of the Pd−M bond. Such a decrease suggests that the coordination number (CN) of Pd atoms in PdCuZn NSs is reduced after Cu/Zn codoping, which leads to the coordinatively unsaturated status of Pd sites. A main peak at 2.45 Å in the FT-EXAFS spectra of the Cu K-edge and a prominent peak of 2.39 Å in the FT-EXAFS spectra of the Zn K-edge in PdCuZn NSs are also observed in Figure S6c,d, assigned to the Cu−M bond and Zn−M bond, respectively. The wavelet transform-EXAFS (WT-EXAFS) pattern of each metal element in PdCuZn NSs was obtained to further provide coordinate information in k and R space, as shown in Figures 2f and S6e,f. The WT-EXAFS spectrum at the Pd K-edge for PdCuZn NSs shows that a maximum intensity at ∼8.45 $Å^{-1}$ in the k-space is resolved at 2.20 Å in the R-space, which is ascribed to Pd−M coordination. In addition, a maximum signal of Cu−M coordination and Zn−M coordination is located at 9.75 and 6.95 $Å^{-1}$, respectively, demonstrating the existence of Pd−Cu/Zn heteroatomic bonds. The FT-EXAFS spectra were fitted using the ARTEMIS module to gain an in-depth understanding of the local structure of the PdCuZn catalysts. The fitting results are shown in Figure S7, and the structural parameters are listed in Table S2. The EXAFS fitting curve of the Pd K-edge reveals that the coordination shell of Pd contains Pd−Cu and Pd−M backscattering paths. The PdCuZn NSs exhibit the Pd−Cu bond with a CN of 1.89 and the Pd−M bond with a CN of 8.64, respectively, which are lower than those in bulk Pd foil (12). The Pd−M bond length is 2.67 Å, which is smaller than the Pd−Pd bond length of bulk materials (2.74 Å), suggesting the presence of compressive strain caused by alloying effects. The EXAFS fitting curve of the Cu K-edge exhibits the Cu−Cu bond with a CN of 1.57 and a bond length of 2.55 Å, slightly larger than the value of bulk Cu (2.53 Å). The EXAFS fitting curve of the Zn K-edge shows that the CN of the Zn−Cu bond is 1.09, and the bond length is 2.57 A, which is less than the value of the metal Zn (2.66 Å). The above analysis results demonstrate the coexistence of lattice strain effects and coordinatively unsaturated Pd sites in PdCuZn NSs after the simultaneous incorporation of Cu and Zn into ultrathin Pd layers, which is conducive to enhancing the catalytic activity.

The electrochemical performances of as-prepared samples for the CO_2RR were measured in a three-compartment flow cell (Figure S8). Different compositions of Cu and Zn in Pd-based electrocatalysts have an important effect on the electrochemical performance of the CO_2RR performance. As-prepared PdCuZn NSs with a Pd/Cu/Zn atomic ratio of 3.99/1.96/1.00 were identified to be the optimum candidate for the CO_2RR due to their high CO selectivity and current density (Figure S9). In addition, PdCu, PdZn, and pure Pd were also tested under the same conditions for comparison. Linear sweep voltammetry (LSV) curves were first recorded under Ar and CO_2 atmospheres. As shown in Figure S10, the LSV curves of PdCuZn, PdCu, and PdZn NSs tested under a CO_2 atmosphere exhibit larger current density and lower onset potential than those tested under an Ar atmosphere in the measured potential range, which suggests that PdCuZn, PdCu, and PdZn NSs are very sensitive to the CO_2RR. Particularly,

https://doi.org/10.1021/jacs.4c14253
J. Am. Chem. Soc. 2025, 147, 4219−4229

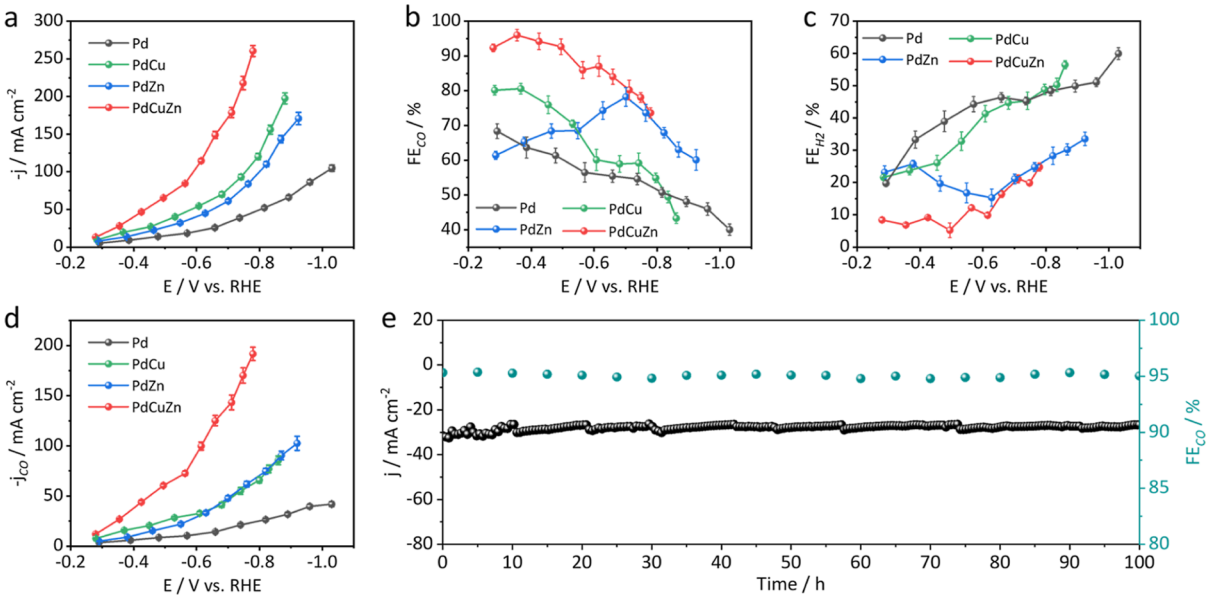

Figure 3. Electrochemical CO_2RR performance. (a) Total current density of PdCuZn, PdCu, PdZn, and Pd NSs for the CO_2RR. (b) FE_{CO} of PdCuZn, PdCu, PdZn, and Pd NSs for the CO_2RR. (c) FE_{H2} of PdCuZn, PdCu, PdZn, and Pd NSs for the CO_2RR. (d) Comparison of CO partial current densities of CO at various potentials. (e) The total current density and FE_{CO} of the PdCuZn NSs over long-term electrolysis.

PdCuZn NSs possess the best catalytic activity under a CO_2 atmosphere among all tested catalysts, indicating the excellent intrinsic CO_2RR activity of PdCuZn NSs. In addition, the LSV curve of Pd NSs displays a lower current density under a CO_2 atmosphere than under an Ar atmosphere, demonstrating that the HER might prevail over the CO_2RR on pure Pd NSs. The total current density of PdCuZn, PdCu, PdZn, and Pd NSs for the CO_2RR is summarized in Figure 3a. PdCuZn NSs display the highest current density (260.4 mA cm^{-2}), notably higher than that of PdCu (197.5 mA cm^{-2}) and PdZn (170.7 mA cm^{-2}), indicating that the cointroduction of Cu and Zn can significantly improve the catalytic activity. Compared with Cu/Zn-doped Pd catalysts, pure Pd exhibits a much lower total current density (104.8 mA cm^{-2}). The FEs of CO_2RR products of PdCuZn, PdCu, PdZn, and Pd NSs under different potentials are shown in Figure S11. Only two gas products (CO and H_2) were identified by gas chromatography (GC), and no liquid products were detected by nuclear magnetic resonance (NMR) after electrolysis (Figures S12 and S13). The FEs of CO_2RR products heavily depend on the applied potentials, and a much higher current density is observed on PdCuZn than the other three catalysts at all potentials. The efficiency diagrams of the CO products of these four catalysts at different potentials are shown in Figure 3b. The PdCuZn NSs exhibit higher FE_{CO} than the other three catalysts under the whole applied potential. Remarkably, the FE_{CO} of PdCuZn NSs exceeds 92% over the potential range of −0.25 to −0.50 V. A maximum FE_{CO} of 96% is obtained at −0.35 V, corresponding to an overpotential of 240 mV, which is comparable to the performance of Pd-based catalysts reported under the same test conditions (Table S3). Moreover, the FE_{CO} exceeds 80% in the range from −0.28 to −0.71 V. By contrast, the FE_{CO} of PdCu, PdZn, and Pd NSs is less than 81% over the applied potentials. The FEs of H_2 of these catalysts under different potentials are shown in Figure 3c. As-prepared PdCuZn NSs display lower FE_{H2} than the other three catalysts under the whole applied potentials. Figure 3d shows the plots of partial current density (j_{CO}) versus the applied potentials of the four catalysts. The j_{CO} of all four catalysts presents an increasing trend as the cathodic potential. Notably, the maximum j_{CO} of PdCuZn NSs is 191.65 mA cm^{-2}, much larger than that of PdCu (85.52 mA cm^{-2}), PdZn (102.56 mA cm^{-2}), and Pd NSs (41.92 mA cm^{-2}).

The electrochemically active surface area (ECSA) is also an important descriptor in dictating the catalytic activity. Therefore, the ECSAs of catalysts were evaluated from the integrated charge of Pd oxide reduction by measuring cyclic voltammetry (CV) curves, as shown in Figure S14. The ECSAs were then calculated to be 40.30, 99.05, 165.24, and 170.00 cm^2 for PdCuZn, PdCu, PdZn, and Pd NSs, respectively. The ECSA and mass-normalized current densities of the four catalysts are shown in Figure S15 to evaluate the intrinsic activity. The Pd-based alloys display enhanced specific and mass activities compared to pure Pd NSs. In particular, PdCuZn NSs have the highest specific activity and mass activity among Pd-based alloys. Specifically, PdCuZn NSs show a specific activity of 4.76 mA cm^{-2} and a mass activity of 277.44 A g^{-1}_{Pd} at −0.78 V. Electrochemical impedance spectroscopy (EIS) was performed to study charge-transfer dynamics in the electrochemical process.[47] As shown in Figure S16, PdCuZn NSs show a smaller ohmic resistance (R_s) of 1.9 Ω and a charge-transfer resistance (R_{ct}) of 3.0 Ω than other Pd-based catalysts, indicating that the coincorporation of Cu and Zn brings in good conductivity and fast charge-transfer dynamics for the electrocatalytic process. The long-term stability of the PdCuZn catalyst was also measured using the chronoamperometry technique method, during which the product analysis from the CO_2RR via GC was done every 5 h. As shown in Figure 3e, the current density displays a negligible deterioration even after 100 h of continuous testing. More remarkably, the FE_{CO} remained so well at ∼95% throughout the entire electrolysis. We further evaluated the long-term durability at −200 mA cm^{-2} using a membrane electrode assembly (MEA) electrolyzer. Specifically, the "PdCuZn/GDL || Ni foam" system exhibits good durability for CO_2RR electrolysis at −200 mA cm^{-2}, which maintains the FE_{CO} at

https://doi.org/10.1021/jacs.4c14253
J. Am. Chem. Soc. 2025, 147, 4219−4229

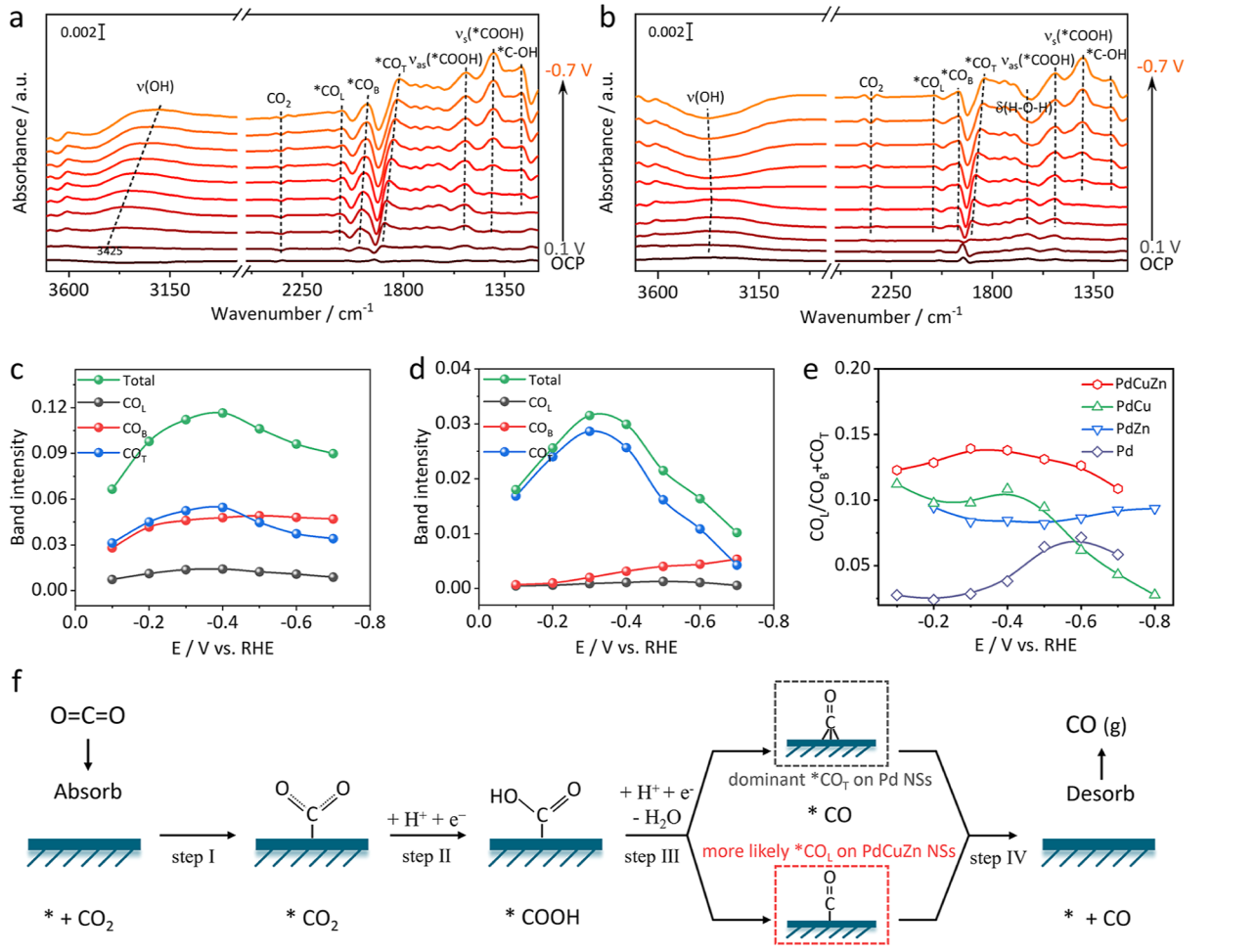

Figure 4. Mechanism insights. In situ ATR-FTIR spectroscopy of (a) PdCuZn and (b) Pd NSs with CO_2 purging. Potential-dependent *CO band intensity of (c) PdCuZn and (d) Pd NSs. (e) $*CO_L$ to $*CO_B$ + $*CO_T$ band intensity ratio. (f) Proposed CO_2RR to the CO process over PdCuZn and pure Pd NSs.

~80% for 45 h with negligible selectivity loss (Figure S17), indicating its potential toward practical applications. Such outstanding performances of long-term electrolysis might be attributed to the strong electronic coupling between multicompetent and unique ultrathin structures, which makes PdCuZn NSs a promising catalyst for practical application toward CO_2-to-CO conversion. Furthermore, PdCuZn after long-term electrolysis was also characterized by XRD, TEM, and XPS (Figures S18−S20). The XRD pattern shows that PdCuZn still maintains a fcc phase. The intensity of the diffraction peak is weaker than before electrolysis, which is caused by the detachment of some catalysts from GDL during the electrolysis process. The TEM image shows that PdCuZn still retains the flexible, corrugated, and ultrathin NS morphology after electrolysis. The HRTEM image also indicates that PdCuZn still maintains a fcc structure with exposed (111) planes. In addition, the EDS elemental mappings manifest that the Pd, Cu, and Zn elements are uniformly distributed throughout the NSs. The XPS spectra indicate that the composition and valence state remain almost unchanged after electrolysis. These results confirm the robust structural stability of the PdCuZn NSs.

In order to gain a deeper understanding of the enhanced activity and CO selectivity upon Cu/Zn incorporation, in situ attenuated total reflectance-Fourier transform infrared (ATR-FTIR) absorption spectroscopy was carried out to monitor the evolution of intermediates on the PdCuZn and Pd NSs under operating conditions (Figure S21). Figure 4a,b shows in situ ATR-FTIR spectra of PdCuZn and Pd NSs under a CO_2 atmosphere, which were recorded during the cathodic scanning process in a CO_2-saturated 0.2 M $KHCO_3$ solution from 0.1 V to −0.7 V. The characteristic bands vary versus bias potentials, which corresponds to the adsorption behavior of reagents and intermediates during the CO_2RR process. A downward band appeared at 2343 cm^{-1} which belongs to CO_2 consumption in the solution.[48] Two positive-going bands at 1410 and 1531 cm^{-1} were observed at 0.1 V, which are assigned to symmetric and asymmetric stretching mode of O−C−O from $*COO^-$, respectively,[49] indicating that the CO_2 activation is facile on the PdCuZn catalyst. A positive-going band appeared at 1280 cm^{-1} and was ascribed to the OH-deformation of the *COOH intermediate.[49] As the cathode potential increases, the characteristic bands at ~2071, 1974, and 1855 cm^{-1} appear at 0 V, ascribed to linearly bound $*CO_L$, bridge-bound $*CO_B$, and triple-bound $*CO_T$, respectively, implying a rapid conversion from *COOH to *CO.[21,50] The *CO band intensity becomes stronger, and the bands shift to lower wavenumbers with the increase of potential. Such a blue shift of *CO bands is induced by Stark effects, which is derived from the changes of the interfacial electric field.[51−53] The

https://doi.org/10.1021/jacs.4c14253
J. Am. Chem. Soc. 2025, 147, 4219−4229

characteristic bands appear in the 3200−3400 cm^{-1} region, corresponding to the stretching vibration of OH from adsorbed H_2O,[54] which is derived from the water generated during the CO_2RR process or from the water in the solution. For in situ ATR-FTIR spectra of Pd NSs, the CO_2 peak (2343 cm^{-1}) appears at −0.1 V, which is more negative than that of the CO_2 peak in PdCuZn NSs, indicating that the CO_2 adsorption on PdCuZn NSs is much easier than on Pd NSs. In addition, the vibration peak intensities of *CO bands (2059 cm^{-1} for $*CO_L$, 1951 cm^{-1} for $*CO_B$, and 1836 cm^{-1} for $*CO_T$) on Pd NSs are weaker than those of PdCuZn NSs between 0 and −0.7 V, indicating PdCuZn NSs are more favorable for CO_2 activation and subsequent conversion toward CO compared with Pd NSs. Particularly, the characteristic bands appear at ∼1645 cm^{-1} in the spectra of Pd NSs, which is assigned to the H−O−H bending vibration mode of H_2O. Meanwhile, the O−H stretching vibration of H_2O also appears at ∼3378 cm^{-1}.[55,56] Remarkably, at lower potentials, the vibrational peaks of H_2O are upward, which is attributed to H_2O produced by the CO_2RR process. However, the vibration peaks of H_2O turn downward as the potential increases, which represents the consumption of H_2O to produce H_2 in the electrolyte. This transition from H_2O production to H_2O consumption indicates that the CO_2RR is dominant on Pd NSs at lower potentials, while the activity of competing H_2O decomposition exceeds that of the CO_2RR at higher potentials. This phenomenon is consistent with the results of electrochemical CO_2RR testing on Pd NSs. In situ ATR-FTIR spectra of PdCu and PdZn NSs are shown in Figure S22a,b, and PdCu and PdZn exhibit typical vibrational peaks similar to PdCuZn and Pd NSs. The CO_2 peaks of PdCu and PdZn appear at −0.1 V. With the appearance of the characteristic CO_2 peak, the vibration peaks of *CO bands ($*CO_L$, $*CO_B$, and $*CO_T$) also begin to appear. However, only $*CO_L$ peaks are obviously observed at −0.1 V for PdZn. As the potential increases, $*CO_B$ and $*CO_T$ bands appear, and the peak intensities gradually increase. In addition, a control experiment of electrolysis under an Ar-saturated 0.2 M $KHCO_3$ solution was further performed to investigate whether the CO_2 reduction activity of PdCuZn NSs comes from CO_2 molecules dissolved in solution or from CO_2 molecules released by bicarbonate ions. As shown in Figure S23, the *CO characteristic band also occurred in the 2000−2100 cm^{-1} region under an Ar atmosphere, but the onset potential of *CO is higher, and the intensity of *CO is rather weaker than that in a CO_2 atmosphere. This weak *CO signal may be derived from the reduction of CO_2 molecules released by bicarbonate ions.[21,57] The above analysis demonstrates that solution-phase CO_2 dominates the CO_2RR of PdCuZn NSs.

The configuration of adsorbed *CO (CO_L, CO_B, or CO_T) on the catalyst surface plays critical roles in determining its binding affinity and desorption rate, in turn dictating the overall performance. Therefore, potential-dependent plots of $*CO_L$, $*CO_B$, and $*CO_T$ areas in the total *CO bands were performed by integration to visualize the adsorption states of *CO on the catalyst surface, as shown in Figures 4c,d and S22c,d. First, PdCuZn NSs exhibit much stronger *CO band intensity compared with those of Pd, PdCu, and PdZn NSs under all selected potentials, indicating that the *CO intermediate more favorably appears on PdCuZn NSs than on other catalysts. The potential-dependent plots of PdCuZn NSs show that obvious *CO intensities begin at −0.1 V and then quickly increase to −0.4 V, reaching a maximum value of 0.12. Importantly, $*CO_B$ and $*CO_T$ show a fair intensity under the entire potential window, far higher than the $*CO_L$ intensity. However, for Pd NSs, the $*CO_T$ dominates and its intensity is much higher than that of $*CO_L$ and $*CO_B$ under the entire potential window (Figure 4d). The potential-dependent integration analysis highlights that PdCuZn NSs are more likely to adopt $*CO_L$ or $*CO_B$ configuration, while pure Pd NSs prefer $*CO_T$ as the dominant configuration when catalyzing the CO_2 to CO process. As a key intermediate for producing CO, the flexible *CO configuration on PdCuZn NSs might explain the enhanced activity and selectivity after the simultaneous incorporation of Cu and Zn. According to previous reports, the sequence of *CO binding energy is $*CO_L$ < $*CO_B$ < $*CO_T$.[21,22,58] Therefore, $*CO_L$ desorption more easily occurs because the binding affinity of $*CO_L$ on Pd sites is weaker than that of $*CO_B$ and $*CO_T$ configuration. Too many $*CO_T$ configurations on Pd sites lead to a strong binding affinity of *CO, which means poisoning of Pd sites, and finally harm the CO production. The quantitative analysis of the $CO_L/(CO_B + CO_T)$ ratios is provided to evaluate the *CO binding strength. As shown in Figure 4e, PdCuZn NSs achieve the highest $CO_L/(CO_B + CO_T)$ ratios compared with Pd, PdCu, and PdZn under all selected potentials. The increasing proportion of weak-binding $*CO_L$ configuration demonstrates enhanced anti-CO-poisoning capability and makes subsequent *CO desorption easy to carry out on PdCuZn NSs, which eventually confers the impressive CO_2-to-CO performance.

$$CO_2 + * \rightarrow *CO_2 \quad \text{(Step 1)}$$

$$*CO_2 + H^+ + e^- \rightarrow *COOH \quad \text{(Step 2)}$$

$$*COOH + H^+ + e^- \rightarrow *CO + H_2O \quad \text{(Step 3)}$$

$$*CO \rightarrow CO(g) + * \quad \text{(Step 4)}$$

Based on the above results, the specific reaction process over PdCuZn NSs for the CO_2RR to the CO products is proposed in Figure 4f. First, CO_2 molecules are absorbed and activated on the PdCuZn NS surface to form $*CO_2$ (Step Step 1). Second, $*CO_2$ is hydrogenated to generate *COOH intermediates (Step Step 2). Then, *CO is formed through the proton-coupled electron transfer (PCET) process (Step Step 3). The *CO on the PdCuZn surface is more likely to choose the $*CO_L$ configurations after Cu and Zn doping, which is totally different from the dominant $*CO_T$ configurations on Pd NSs. Such evolving tendencies on the *CO configurations highlight the significance of electronic modulation via the Cu and Zn coincorporation. Finally, CO gas molecules are generated due to facile *CO desorption from the active sites of the catalyst surface (Step Step 4).

Density functional theory (DFT) calculations were performed to gain in-depth insight into the enhanced catalytic mechanism toward CO_2-to-CO conversion. First, the simulated structural models were constructed upon the fcc structure, which exposes (111) facets according to the TEM and XRD results. The modeling details are described in the Supporting Information, and the specific structural models of Pd, PdZn, PdCu, and PdCuZn are shown in Figure S24. Considering that there are three metal elements in PdCuZn, we first calculated the reaction pathways and free energies on Cu, Zn, and Pd sites of PdCuZn to determine the true active sites toward the CO_2RR to CO process. For the CO_2RR to CO process over both the Cu site and Pd site, the $*CO_2$ absorption

https://doi.org/10.1021/jacs.4c14253
J. Am. Chem. Soc. 2025, 147, 4219−4229

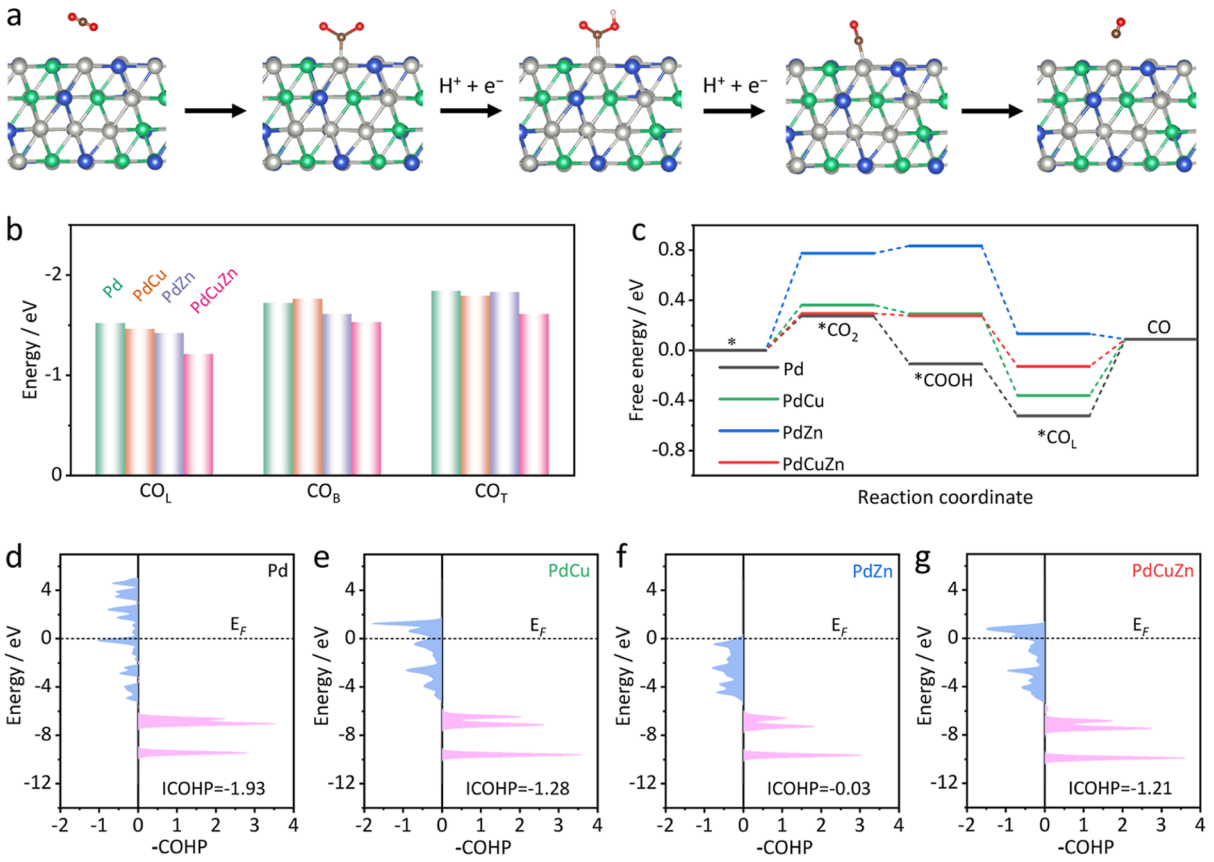

Figure 5. DFT simulations. (a) Reaction pathway of the CO_2RR to CO over PdCuZn NSs (the adsorption of *CO intermediates displayed here is $*CO_L$). (b) Adsorption energies of CO_L, CO_B, and CO_T on Pd, PdCu, PdZn, and PdCuZn. (c) Free energy diagrams of Pd, PdCu, PdZn, and PdCuZn via the $*CO_L$ configuration. (d–g) COHP plots of different catalysts. Light purple represents the bonding state, and light blue represents the antibonding state.

is the rate-determining step, which requires free energies of 0.38 and 0.29 eV on Cu and Pd sites, respectively. For the Zn site, the $*CO_2$ hydrogenation to *COOH formation is the rate-determining step, which gives an increased energy barrier of 0.53 eV, thus limiting the CO_2-to-CO conversion on the Zn site (Figure S25). Since the Pd sites of the PdCuZn surface exhibit the lowest energy barrier for the CO_2RR to CO, the surface Pd sites of PdCuZn act as the most active sites for the CO_2RR to CO.

The reaction pathway for the CO_2RR to CO over PdCuZn is shown in Figure 5a, and the atomic configurations of adsorbates on the Pd sites of Pd, PdZn, and PdCu are shown in Figure S26, in which CO_2 is converted to CO through the following elementary reaction steps including CO_2 absorption, CO_2 activation to *COOH, *CO formation, and *CO desorption. First, the *CO adsorption configurations (CO_L, CO_B, and CO_T) on the surface of Pd, PdZn, PdCu, and PdCuZn were studied by DFT calculations. Specific structural models are shown in Figure S27. The corresponding adsorption energies of $*CO_L$, $*CO_B$, and $*CO_T$ on Pd, PdCu, PdZn, and PdCuZn were summarized and are shown in Figure 5b. The $*CO_L$ absorption configuration on the surface of Pd, PdZn, PdCu, and PdCuZn exhibits the lowest binding affinity, indicating that $*CO_L$ is more easily desorbed compared with $*CO_B$ and $*CO_T$. Moreover, PdCuZn displays more positive adsorption energies for the three kinds of *CO adsorption than pure Pd, PdCu, and PdZn, indicating the weaker *CO absorption strength on the surface of PdCuZn than pure Pd, PdCu and PdZn.

The free energetics on Pd, PdCu, PdZn, and PdCuZn via the $*CO_L$, $*CO_B$, and $*CO_T$ configurations for the CO_2RR to CO were further calculated and are shown in Figures 5c and S28. The calculated Gibbs free energies of CO_2 (ΔG_{*CO_2}) on Pd sites over all catalysts are positive values (0.29, 0.36, 0.78, and 0.27 eV for PdCuZn, PdCu, PdZn, and Pd, respectively), indicating that the absorption of CO_2 on active sites is the potential-determining step and PdCuZn could achieve CO_2 absorption under lower potential compared with the bimetallic counterparts. The following *COOH formation (ΔG_{*COOH}) reveals an exothermic step over Pd (−0.11 eV), PdCu (0.29 eV), and PdCuZn (0.27 eV), while it is endothermic on PdZn (0.84 eV). Then, the free energy pathways to *CO formation through PCET are thermodynamically downhill over all catalysts, implying that the *CO formation spontaneously happens over all catalysts. The subsequent *CO species are desorbed from the catalyst surface via the $*CO_L$, $*CO_B$, and $*CO_T$ configurations. Obviously, the desorption energy barriers of $*CO_L$ species are much lower than those of $*CO_B$ and $*CO_T$ species for all four catalysts, suggesting that the $*CO_L$ configuration is more active than the other two configurations toward the formation of the gaseous CO product.

Specifically, PdZn shows the lowest energy barrier for $*CO_L$, $*CO_B$, and $*CO_T$ desorption to release CO (g), while the larger energy barrier of $*CO_2$ absorption (0.84 eV) limits its

https://doi.org/10.1021/jacs.4c14253
J. Am. Chem. Soc. 2025, 147, 4219−4229

CO_2RR to CO production. The desorption of $*CO_L$, $*CO_B$, and $*CO_T$ species to form CO (g) on Pd, PdCu, and PdCuZn is found to be thermodynamically uphill. Compared with PdCu and Pd, PdCuZn exhibits the lowest energy barrier for $*CO_L$, $*CO_B$, and $*CO_T$ desorption to produce CO (g). These results also indicate that no matter what *CO configuration is adopted during the CO_2RR to CO, PdCuZn always exhibits the lowest energy barrier for the CO_2-to-CO conversion when compared with other Pd-based counterparts, implying that the bimetallic doping strategy is effective in facilitating the CO_2RR to CO production.

The projected density of states (PDOS) was then calculated to investigate the adsorption and binding behaviors of intermediates upon the electronic structures. As is shown in Figure S29, the d-band centers of PdCuZn (3.18 eV), PdCu (2.12 eV), and PdZn (2.99 eV) display a downward shift relative to the pure Pd (1.80 eV), in good conformity with the VB-XPS analysis. And the PDOSs of each element in PdCuZn reveal their electronic contributions and confirm the existence of strong electronic coupling (Figure S30a). In addition, Bader charge analysis of PdCuZn shows that the charge state of Pd is positive, while the charge states of Cu and Zn are negative (Figure S30b), also suggesting strong electronic coupling between multicomponent elements.

In order to further study the bonding properties between Pd sites and *CO species, we calculated the crystal orbital Hamilton population (COHP) between Pd active sites and *CO.[59,60] As shown in Figure 5d−g, the antibonding orbitals below the Fermi level in PdCu, PdZn, and PdCuZn are more occupied than pure Pd, signifying the weak bonding strengths between Pd sites and *CO in PdCu, PdZn, and PdCuZn. The orbital overlaps and bonding strengths between Pd and *CO were further quantitatively analyzed by integrated COHP (ICOHP), which is computed by integrating the COHP up to the Fermi level. The ICOHP values of Pd, PdCu, PdZn, and PdCuZn are −1.93, −1.28, −0.03, and −1.21 eV, respectively. The increased ICOHP values further demonstrate the weaker bonding strengths between Pd sites and *CO in PdCu, PdZn, and PdCuZn compared with pure Pd. Furthermore, CO stripping measurements were carried out to experimentally study the absorption of CO on as-prepared catalysts. As shown in Figure S31, the PdCuZn NSs exhibit an obvious shift of the CO oxidation peak (~27 mV shift to lower potentials) and a dramatical increase of peak intensity, confirming the weaker CO adsorption and higher CO resistance on PdCuZn NSs than that of pure Pd NSs. The combined results of DFT simulations and CO stripping experiments emphasize that the interaction between Pd and adsorbed CO is prominently diminished after the codoping of Cu and Zn into the Pd lattice, thereby expediting the CO desorption and facilitating the conversion of CO_2RR to CO.

3. CONCLUSIONS

In summary, ultrathin Pd-alloy electrocatalysts with alleviated *CO binding affinity have been subtly designed and synthesized for efficient CO_2-to-CO conversion. Simultaneous codoping of Cu and Zn into the Pd atomic layer generates more effective outcomes for fine control of the catalyst's electronic structure when compared with the bimetallic PdCu, PdZn, and pure Pd NSs. The as-resulted PdCuZn NSs with few atomic layers exhibit highly selective CO production under an extended potential window, achieving an optimal FE_{CO} of 96% at −0.35 V (vs RHE). The PdCuZn electrode also maintains a CO production of ~95% FE_{CO} during 100 h electrolysis, revealing its potential for practical CO_2RR applications. In situ electrochemical ATR-FTIR spectroscopy measurements manifest a fast *CO desorption process over PdCuZn NSs due to the selected adoption of a weakly bound $*CO_L$ configuration on the NS surface, leading to the enhanced anti-CO-poisoning capability. DFT calculations confirm that coincorporation of Cu and Zn into the Pd lattice produces a more reasonable electronic structure and lower d-band center of active sites, which effectively tailors the adsorption configuration of intermediates and decreases the energy barrier of rate-determining *CO desorption, thereby accelerating the CO_2-to-CO conversion. This study highlights a principle for designing and synthesizing Pd-based alloy electrocatalysts, in which the bimetallic codoping tactic enables precise modification of adsorption configurations to meet the appetite of selective CO_2RR applications.

■ ASSOCIATED CONTENT

Supporting Information

The Supporting Information is available free of charge at https://pubs.acs.org/doi/10.1021/jacs.4c14253.

Detailed experimental and calculation information, additional material characterizations, electrochemical data, and theoretical simulation data (PDF)

■ AUTHOR INFORMATION

Corresponding Authors

Xiao Zhang − *Department of Mechanical Engineering and Research Institute for Advanced Manufacturing, The Hong Kong Polytechnic University, Kowloon 999077 Hong Kong, China*; orcid.org/0000-0002-4780-2161; Email: xiao1.zhang@polyu.edu.hk

Kangcheung Chan − *Department of Industrial and Systems Engineering and Research Institute for Advanced Manufacturing, The Hong Kong Polytechnic University, Kowloon 999077 Hong Kong, China*; orcid.org/0000-0002-6173-5532; Email: kc.chan@polyu.edu.hk

Authors

Shuting Wei − *Department of Industrial and Systems Engineering and Department of Mechanical Engineering, The Hong Kong Polytechnic University, Kowloon 999077 Hong Kong, China*

Yanchao Xu − *Department of Industrial and Systems Engineering, The Hong Kong Polytechnic University, Kowloon 999077 Hong Kong, China*

Tao Song − *Department of Chemistry, Southern University of Science and Technology, Shenzhen 518055, China*

Hao Dai − *Department of Chemistry, Southern University of Science and Technology, Shenzhen 518055, China*

Fan Li − *Department of Chemistry, Southern University of Science and Technology, Shenzhen 518055, China*

Xin Gao − *Department of Mechanical Engineering, The Hong Kong Polytechnic University, Kowloon 999077 Hong Kong, China*

Yanjie Zhai − *Department of Mechanical Engineering, The Hong Kong Polytechnic University, Kowloon 999077 Hong Kong, China*

Shanhe Gong − *Department of Mechanical Engineering, The Hong Kong Polytechnic University, Kowloon 999077 Hong Kong, China*

https://doi.org/10.1021/jacs.4c14253
J. Am. Chem. Soc. 2025, 147, 4219−4229

Rui Li − *Institute of Clean Energy, Yangtze River Delta Research Institute, Northwestern Polytechnical University, Xi'an 710072, China;* orcid.org/0000-0002-8654-090X

Complete contact information is available at: https://pubs.acs.org/10.1021/jacs.4c14253

Author Contributions

All authors have given approval to the final version of the manuscript.

Notes

The authors declare no competing financial interest.

■ ACKNOWLEDGMENTS

The authors greatly appreciate the support from the Research Institute for Advanced Manufacturing (RIAM) of The Hong Kong Polytechnic University (Project numbers: 1-CD4L and 1-CD9B).

■ REFERENCES

(1) De Luna, P.; Hahn, C.; Higgins, D.; Jaffer, S. A.; Jaramillo, T. F.; Sargent, E. H. What would it take for renewably powered electrosynthesis to displace petrochemical processes? *Science* **2019**, *364*, No. eaav3506.

(2) Chu, S.; Cui, Y.; Liu, N. The path towards sustainable energy. *Nat. Mater.* **2017**, *16*, 16−22.

(3) Birdja, Y. Y.; Pérez-Gallent, E.; Figueiredo, M. C.; Göttle, A. J.; Calle-Vallejo, F.; Koper, M. T. M. Advances and challenges in understanding the electrocatalytic conversion of carbon dioxide to fuels. *Nat. Energy* **2019**, *4*, 732−745.

(4) Xue, J.; Dong, X.; Liu, C.; Li, J.; Dai, Y.; Xue, W.; Luo, L.; Ji, Y.; Zhang, X.; Li, X.; Jiang, Q.; Zheng, T.; Xiao, J.; Xia, C. Turning copper into an efficient and stable CO evolution catalyst beyond noble metals. *Nat. Commun.* **2024**, *15*, 5998.

(5) Kim, J. Y. T.; Sellers, C.; Hao, S.; Senftle, T. P.; Wang, H. Different distributions of multi-carbon products in CO_2 and CO electroreduction under practical reaction conditions. *Nat. Catal.* **2023**, *6*, 1115−1124.

(6) Zhang, L.; Feng, J.; Wu, L.; Ma, X.; Song, X.; Jia, S.; Tan, X.; Jin, X.; Zhu, Q.; Kang, X.; Ma, J.; Qian, Q.; Zheng, L.; Sun, X.; Han, B. Oxophilicity-Controlled CO_2 Electroreduction to C_{2+} Alcohols over Lewis Acid Metal-Doped $Cu^{\delta+}$ Catalysts. *J. Am. Chem. Soc.* **2023**, *145*, 21945−21954.

(7) Dai, Y.; Li, H.; Wang, C.; Xue, W.; Zhang, M.; Zhao, D.; Xue, J.; Li, J.; Luo, L.; Liu, C.; Li, X.; Cui, P.; Jiang, Q.; Zheng, T.; Gu, S.; Zhang, Y.; Xiao, J.; Xia, C.; Zeng, J. Manipulating local coordination of copper single atom catalyst enables efficient CO_2-to-CH_4 conversion. *Nat. Commun.* **2023**, *14*, 3382.

(8) Wang, B.; Wang, M.; Fan, Z.; Ma, C.; Xi, S.; Chang, L. Y.; Zhang, M.; Ling, N.; Mi, Z.; Chen, S.; Leow, W. R.; Zhang, J.; Wang, D.; Lum, Y. Nanocurvature-induced field effects enable control over the activity of single-atom electrocatalysts. *Nat. Commun.* **2024**, *15*, 1719.

(9) Chen, Z.; Wang, C.; Zhong, X.; Lei, H.; Li, J.; Ji, Y.; Liu, C.; Ding, M.; Dai, Y.; Li, X.; Zheng, T.; Jiang, Q.; Peng, H. J.; Xia, C. Achieving Efficient CO_2 Electrolysis to CO by Local Coordination Manipulation of Nickel Single-Atom Catalysts. *Nano Lett.* **2023**, *23*, 7046−7053.

(10) Chen, Y.; Li, X. Y.; Chen, Z.; Ozden, A.; Huang, J. E.; Ou, P.; Dong, J.; Zhang, J.; Tian, C.; Lee, B. H.; Wang, X.; Liu, S.; Qu, Q.; Wang, S.; Xu, Y.; Miao, R. K.; Zhao, Y.; Liu, Y.; Qiu, C.; Abed, J.; Liu, H.; Shin, H.; Wang, D.; Li, Y.; Sinton, D.; Sargent, E. H. Efficient multicarbon formation in acidic CO_2 reduction via tandem electrocatalysis. *Nat. Nanotechnol.* **2024**, *19*, 311−318.

(11) Zhu, P.; Wang, H. High-purity and high-concentration liquid fuels through CO_2 electroreduction. *Nat. Catal.* **2021**, *4*, 943−951.

(12) Hao, J.; Zhuang, Z.; Hao, J.; Cao, K.; Hu, Y.; Wu, W.; Lu, S.; Wang, C.; Zhang, N.; Wang, D.; Du, M.; Zhu, H. Strain Relaxation in Metal Alloy Catalysts Steers the Product Selectivity of Electrocatalytic CO_2 Reduction. *ACS Nano* **2022**, *16*, 3251−3263.

(13) Jin, S.; Hao, Z.; Zhang, K.; Yan, Z.; Chen, J. Advances and Challenges for the Electrochemical Reduction of CO_2 to CO: From Fundamentals to Industrialization. *Angew. Chem., Int. Ed.* **2021**, *60*, 20627−20648.

(14) Han, N.; Ding, P.; He, L.; Li, Y.; Li, Y. Promises of Main Group Metal-Based Nanostructured Materials for Electrochemical CO_2 Reduction to Formate. *Adv. Energy Mater.* **2019**, *10*, 1902338.

(15) Sheng, W.; Kattel, S.; Yao, S.; Yan, B.; Liang, Z.; Hawxhurst, C. J.; Wu, Q.; Chen, J. G. Electrochemical reduction of CO_2 to synthesis gas with controlled CO/H_2 ratios. *Energy Environ. Sci.* **2017**, *10*, 1180−1185.

(16) Lin, R.; Ma, X.; Cheong, W.-C.; Zhang, C.; Zhu, W.; Pei, J.; Zhang, K.; Wang, B.; Liang, S.; Liu, Y.; Zhuang, Z.; Yu, R.; Xiao, H.; Li, J.; Wang, D.; Peng, Q.; Chen, C.; Li, Y. PdAg bimetallic electrocatalyst for highly selective reduction of CO_2 with low COOH* formation energy and facile CO desorption. *Nano Res.* **2019**, *12*, 2866−2871.

(17) Tackett, B. M.; Lee, J. H.; Chen, J. G. Electrochemical Conversion of CO_2 to Syngas with Palladium-Based Electrocatalysts. *Acc. Chem. Res.* **2020**, *53*, 1535−1544.

(18) Lee, J. H.; Kattel, S.; Jiang, Z.; Xie, Z.; Yao, S.; Tackett, B. M.; Xu, W.; Marinkovic, N. S.; Chen, J. G. Tuning the activity and selectivity of electroreduction of CO_2 to synthesis gas using bimetallic catalysts. *Nat. Commun.* **2019**, *10*, 3724.

(19) Ding, J.; Li, F.; Ren, X.; Liu, Y.; Li, Y.; Shen, Z.; Wang, T.; Wang, W.; Wang, Y. G.; Cui, Y.; Yang, H.; Zhang, T.; Liu, B. Molecular tuning boosts asymmetric C-C coupling for CO conversion to acetate. *Nat. Commun.* **2024**, *15*, 3641.

(20) Bai, H.; Cheng, T.; Li, S.; Zhou, Z.; Yang, H.; Li, J.; Xie, M.; Ye, J.; Ji, Y.; Li, Y.; Zhou, Z.; Sun, S.; Zhang, B.; Peng, H. Controllable CO adsorption determines ethylene and methane productions from CO_2 electroreduction. *Sci. Bull.* **2021**, *66*, 62−68.

(21) Zhu, S.; Wang, Q.; Qin, X.; Gu, M.; Tao, R.; Lee, B. P.; Zhang, L.; Yao, Y.; Li, T.; Shao, M. Tuning Structural and Compositional Effects in Pd-Au Nanowires for Highly Selective and Active CO_2 Electrochemical Reduction Reaction. *Adv. Energy Mater.* **2018**, *8*, 1802238.

(22) Herron, J. A.; Tonelli, S.; Mavrikakis, M. Atomic and molecular adsorption on Pd(111). *Surf. Sci.* **2012**, *606*, 1670−1679.

(23) Li, M.; Garg, S.; Chang, X.; Ge, L.; Li, L.; Konarova, M.; Rufford, T. E.; Rudolph, V.; Wang, G. Toward Excellence of Transition Metal-Based Catalysts for CO_2 Electrochemical Reduction: An Overview of Strategies and Rationales. *Small Methods* **2020**, *4*, 2000033.

(24) Fan, J.; Du, H.; Zhao, Y.; Wang, Q.; Liu, Y.; Li, D.; Feng, J. Recent Progress on Rational Design of Bimetallic Pd Based Catalysts and Their Advanced Catalysis. *ACS Catal.* **2020**, *10*, 13560−13583.

(25) Nguyen, D. L. T.; Nguyen, T. M.; Lee, S. Y.; Kim, J.; Kim, S. Y.; Le, Q. V.; Varma, R. S.; Hwang, Y. J. Electrochemical conversion of CO_2 to value-added chemicals over bimetallic Pd-based nanostructures: Recent progress and emerging trends. *Environ. Res.* **2022**, *211*, 113116.

(26) Xu, B.; Zhang, Y.; Li, L.; Shao, Q.; Huang, X. Recent progress in low-dimensional palladium-based nanostructures for electrocatalysis and beyond. *Coord. Chem. Rev.* **2022**, *459*, 214388.

(27) Hammer, B.; Norskov, J. K. Why gold is the noblest of all the metals. *Nature* **1995**, *376*, 238−240.

(28) Norskov, J. K.; Abild-Pedersen, F.; Studt, F.; Bligaard, T. Density functional theory in surface chemistry and catalysis. *Proc. Natl. Acad. Sci. U.S.A.* **2011**, *108*, 937−943.

(29) Chen, D.; Yao, Q.; Cui, P.; Liu, H.; Xie, J.; Yang, J. Tailoring the Selectivity of Bimetallic Copper-Palladium Nanoalloys for Electrocatalytic Reduction of CO_2 to CO. *ACS Appl. Energy Mater.* **2018**, *1*, 883−890.

(30) Yin, Z.; Gao, D.; Yao, S.; Zhao, B.; Cai, F.; Lin, L.; Tang, P.; Zhai, P.; Wang, G.; Ma, D.; Bao, X. Highly selective palladium-copper bimetallic electrocatalysts for the electrochemical reduction of CO_2 to CO. *Nano Energy* **2016**, *27*, 35−43.
(31) Zeng, Q.; Tian, S.; Liu, H.; Xu, L.; Cui, P.; Chen, D.; Wang, J.; Yang, J. Fine AgPd Nanoalloys Achieving Size and Ensemble Synergy for High-Efficiency CO_2 to CO Electroreduction. *Adv. Funct. Mater.* **2023**, *33*, 2307444.
(32) Abdinejad, M.; Subramanian, S.; Motlagh, M. K.; Noroozifar, M.; Duangdangchote, S.; Neporozhnii, I.; Ripepi, D.; Pinto, D.; Li, M.; Tang, K.; Middelkoop, J.; Urakawa, A.; Voznyy, O.; Kraatz, H. B.; Burdyny, T. Insertion of MXene-Based Materials into Cu-Pd 3D Aerogels for Electroreduction of CO_2 to Formate. *Adv. Energy Mater.* **2023**, *13*, 2300402.
(33) Luo, M.; Zhao, Z.; Zhang, Y.; Sun, Y.; Xing, Y.; Lv, F.; Yang, Y.; Zhang, X.; Hwang, S.; Qin, Y.; Ma, J. Y.; Lin, F.; Su, D.; Lu, G.; Guo, S. PdMo bimetallene for oxygen reduction catalysis. *Nature* **2019**, *574*, 81−85.
(34) Lin, F.; Lv, F.; Zhang, Q.; Luo, H.; Wang, K.; Zhou, J.; Zhang, W.; Zhang, W.; Wang, D.; Gu, L.; Guo, S. Local Coordination Regulation through Tuning Atomic-Scale Cavities of Pd Metallene toward Efficient Oxygen Reduction Electrocatalysis. *Adv. Mater.* **2022**, *34*, 2202084.
(35) Lv, F.; Huang, B.; Feng, J.; Zhang, W.; Wang, K.; Li, N.; Zhou, J.; Zhou, P.; Yang, W.; Du, Y.; Su, D.; Guo, S. A highly efficient atomically thin curved PdIr bimetallene electrocatalyst. *Natl. Sci. Rev.* **2021**, *8*, nwab019.
(36) Wang, J.; Tan, H. Y.; Zhu, Y.; Chu, H.; Chen, H. M. Linking the Dynamic Chemical State of Catalysts with the Product Profile of Electrocatalytic CO_2 Reduction. *Angew. Chem., Int. Ed.* **2021**, *60*, 17254−17267.
(37) Kuhl, K. P.; Hatsukade, T.; Cave, E. R.; Abram, D. N.; Kibsgaard, J.; Jaramillo, T. F. Electrocatalytic conversion of carbon dioxide to methane and methanol on transition metal surfaces. *J. Am. Chem. Soc.* **2014**, *136*, 14107−14113.
(38) Zhao, L.; Xu, C.; Su, H.; Liang, J.; Lin, S.; Gu, L.; Wang, X.; Chen, M.; Zheng, N. Single-Crystalline Rhodium Nanosheets with Atomic Thickness. *Adv. Sci.* **2015**, *2*, 1500100.
(39) Zhang, Z.; Liu, Y.; Chen, B.; Gong, Y.; Gu, L.; Fan, Z.; Yang, N.; Lai, Z.; Chen, Y.; Wang, J.; Huang, Y.; Sindoro, M.; Niu, W.; Li, B.; Zong, Y.; Yang, Y.; Huang, X.; Huo, F.; Huang, W.; Zhang, H. Submonolayered Ru Deposited on Ultrathin Pd Nanosheets used for Enhanced Catalytic Applications. *Adv. Mater.* **2016**, *28*, 10282−10286.
(40) Huang, X.; Tang, S.; Mu, X.; Dai, Y.; Chen, G.; Zhou, Z.; Ruan, F.; Yang, Z.; Zheng, N. Freestanding palladium nanosheets with plasmonic and catalytic properties. *Nat. Nanotechnol.* **2011**, *6*, 28−32.
(41) Wakisaka, M.; Mitsui, S.; Hirose, Y.; Kawashima, K.; Uchida, H.; Watanabe, M. Electronic structures of Pt-Co and Pt-Ru alloys for CO-tolerant anode catalysts in polymer electrolyte fuel cells studied by EC-XPS. *J. Phys. Chem. B* **2006**, *110*, 23489−23496.
(42) Jiao, S.; Fu, X.; Huang, H. Descriptors for the Evaluation of Electrocatalytic Reactions: d-Band Theory and Beyond. *Adv. Funct. Mater.* **2022**, *32*, 2107651.
(43) Hu, Q.; Gao, K.; Wang, X.; Zheng, H.; Cao, J.; Mi, L.; Huo, Q.; Yang, H.; Liu, J.; He, C. Subnanometric Ru clusters with upshifted D band center improve performance for alkaline hydrogen evolution reaction. *Nat. Commun.* **2022**, *13*, 3958.
(44) Lv, Y.; Lin, L.; Xue, R.; Zhang, P.; Ma, F.; Gan, T.; Zhang, J.; Gao, D.; Zheng, X.; Wang, L.; Qin, Y.; Zhao, H.; Dong, Y.; Wang, Y.; Zhu, Y. Electronegativity Induced d-Band Center Offset for Pt-Rh Dual Sites in High-Entropy Alloy Boosts Liquid Fuels Electrooxidation. *Adv. Energy Mater.* **2024**, *14*, 2304515.
(45) Hou, Z.; Cui, C.; Li, Y.; Gao, Y.; Zhu, D.; Gu, Y.; Pan, G.; Zhu, Y.; Zhang, T. Lattice-Strain Engineering for Heterogenous Electrocatalytic Oxygen Evolution Reaction. *Adv. Mater.* **2023**, *35*, No. e2209876.
(46) Xia, Z.; Guo, S. Strain engineering of metal-based nanomaterials for energy electrocatalysis. *Chem. Soc. Rev.* **2019**, *48*, 3265−3278.
(47) Aniskevich, Y.; Yu, J. H.; Kim, J. Y.; Komaba, S.; Myung, S. T. Tracking Sodium Cluster Dynamics in Hard Carbon with a Low Specific Surface Area for Sodium-Ion Batteries. *Adv. Energy Mater.* **2024**, *14*, 2304300.
(48) Hossain, M. N.; Wen, J.; Konda, S. K.; Govindhan, M.; Chen, A. Electrochemical and FTIR spectroscopic study of CO_2 reduction at a nanostructured Cu/reduced graphene oxide thin film. *Electrochem. Commun.* **2017**, *82*, 16−20.
(49) Firet, N. J.; Smith, W. A. Probing the Reaction Mechanism of CO_2 Electroreduction over Ag Films via Operando Infrared Spectroscopy. *ACS Catal.* **2017**, *7*, 606−612.
(50) Miyake, H.; Hosono, E.; Osawa, M.; Okada, T. Surface-enhanced infrared absorption spectroscopy using chemically deposited Pd thin film electrodes. *Chem. Phys. Lett.* **2006**, *428*, 451−456.
(51) Chen, J.; Fan, L.; Zhao, Y.; Yang, H.; Wang, D.; Hu, B.; Xi, S.; Wang, L. Enhancing Cu-ligand interaction for efficient CO_2 reduction towards multi-carbon products. *Chem. Commun.* **2024**, *60*, 3178−3181.
(52) Wang, Y. M.; Yan, F. Q.; Wang, Q. Y.; Du, C. X.; Wang, L. Y.; Li, B.; Wang, S.; Zang, S. Q. Single-atom tailored atomically-precise nanoclusters for enhanced electrochemical reduction of CO_2-to-CO activity. *Nat. Commun.* **2024**, *15*, 1843.
(53) Wu, Z. Z.; Zhang, X. L.; Niu, Z. Z.; Gao, F. Y.; Yang, P. P.; Chi, L. P.; Shi, L.; Wei, W. S.; Liu, R.; Chen, Z.; Hu, S.; Zheng, X.; Gao, M. R. Identification of Cu(100)/Cu(111) Interfaces as Superior Active Sites for CO Dimerization During CO_2 Electroreduction. *J. Am. Chem. Soc.* **2022**, *144*, 259−269.
(54) Wei, X.; Yin, Z.; Lyu, K.; Li, Z.; Gong, J.; Wang, G.; Xiao, L.; Lu, J.; Zhuang, L. Highly selective reduction of CO_2 to C_{2+} hydrocarbons at copper/polyaniline interfaces. *ACS Catal.* **2020**, *10*, 4103−4111.
(55) Max, J.-J.; Chapados, C. Isotope effects in liquid water by infrared spectroscopy. III. H_2O and D_2O spectra from 6000 to 0 cm^{-1}. *J. Chem. Phys.* **2009**, *131*, 184505.
(56) Chen, S.; Chen, A. Electrochemical Reduction of Carbon Dioxide on Au Nanoparticles: An in Situ FTIR Study. *J. Phys. Chem. C* **2019**, *123*, 23898−23906.
(57) Zhu, S.; Jiang, B.; Cai, W. B.; Shao, M. Direct Observation on Reaction Intermediates and the Role of Bicarbonate Anions in CO_2 Electrochemical Reduction Reaction on Cu Surfaces. *J. Am. Chem. Soc.* **2017**, *139*, 15664−15667.
(58) Jiang, B.; Zhang, X. G.; Jiang, K.; Wu, D. Y.; Cai, W. B. Boosting Formate Production in Electrocatalytic CO_2 Reduction over Wide Potential Window on Pd Surfaces. *J. Am. Chem. Soc.* **2018**, *140*, 2880−2889.
(59) Yuan, K.; Zhang, H.; Gu, Q.; Xiao, T.; Li, Z.; Wong-Ng, W. K.; Zhou, W.; Wang, C.; Wang, S.; Liu, W. Enhanced magnetism in Ru-doped hybrid improper perovskite $Ca_3Mn_2O_7$ via experimental and first-principles study. *J. Am. Ceram. Soc.* **2023**, *106*, 2455−2465.
(60) Wang, J.; Song, Y.; Chen, C.; Zhao, X.; Fan, W. Trade-Off between the Coordination Environment and Active-Site Density on Fe-N_xC_y-C Catalysts for Enhanced Electrochemical CO_2 Reduction to CO. *ACS Catal.* **2023**, *13*, 15794−15810.

https://doi.org/10.1021/jacs.4c14253
J. Am. Chem. Soc. 2025, 147, 4219−4229